



Ferrón, H. G., Martínez-Pérez, C., Rahman, I. A., Selles de Lucas, V., Botella, H., & Donoghue, P. C. J. (2020). Computational fluid dynamics suggests ecological diversification among stem-gnathostomes. *Current Biology*, 30(23), 4808-4813.e3.  
<https://doi.org/10.1016/j.cub.2020.09.031>

Peer reviewed version

License (if available):  
CC BY-NC-ND

Link to published version (if available):  
[10.1016/j.cub.2020.09.031](https://doi.org/10.1016/j.cub.2020.09.031)

[Link to publication record in Explore Bristol Research](#)  
PDF-document

This is the author accepted manuscript (AAM). The final published version (version of record) is available online via Elsevier at [https://www.cell.com/current-biology/fulltext/S0960-9822\(20\)31362-2?\\_returnURL=https%3A%2F%2Flinkinghub.elsevier.com%2Fretrieve%2Fpii%2FS0960982220313622%3Fshowall%3Dtrue](https://www.cell.com/current-biology/fulltext/S0960-9822(20)31362-2?_returnURL=https%3A%2F%2Flinkinghub.elsevier.com%2Fretrieve%2Fpii%2FS0960982220313622%3Fshowall%3Dtrue) . Please refer to any applicable terms of use of the publisher.

## University of Bristol - Explore Bristol Research

### General rights

This document is made available in accordance with publisher policies. Please cite only the published version using the reference above. Full terms of use are available:  
<http://www.bristol.ac.uk/red/research-policy/pure/user-guides/ebr-terms/>

1 **Computational Fluid Dynamics Suggests Ecological Diversification among Stem-**  
2 **Gnathostomes**

3

4 Humberto G. Ferrón,<sup>1,2,5,\*</sup> Carlos Martínez-Pérez,<sup>1,2</sup> Imran A. Rahman,<sup>3</sup> Víctor Selles de  
5 Lucas,<sup>4</sup> Héctor Botella,<sup>2</sup> and Philip C. J. Donoghue,<sup>1,\*</sup>

6

7 <sup>1</sup>School of Earth Sciences, University of Bristol, Life Sciences Building, Tyndall Avenue, Bristol  
8 BS8 1TQ, UK.

9 <sup>2</sup>Instituto Cavanilles de Biodiversidad i Biología Evolutiva, Universitat de València, C/  
10 Catedrático José Beltrán Martínez, 2, 46980 Paterna, Valencia, Spain.

11 <sup>3</sup>Oxford University Museum of Natural History, Parks Road, Oxford OX1 3PW, UK.

12 <sup>4</sup>School of Engineering and Computer Science, University of Hull, Cottingham Rd, Hull HU6  
13 7RX, UK.

14 <sup>5</sup>Lead Contact

15

16 \*Correspondence: [humberto.ferron@bristol.ac.uk](mailto:humberto.ferron@bristol.ac.uk), [phil.donoghue@bristol.ac.uk](mailto:phil.donoghue@bristol.ac.uk)

17

18

19

20

21

22

23

24

## 25 SUMMARY

26 The evolutionary assembly of the vertebrate bodyplan has been characterised as a long-  
27 term ecological trend towards increasingly active and predatory lifestyles, culminating in  
28 jawed vertebrates which dominate modern vertebrate biodiversity [1–8]. This contrast is  
29 no more stark than between the earliest jawed vertebrates and their immediate relatives,  
30 the extinct jawless, dermal armour-encased osteostracans, which have conventionally been  
31 interpreted as benthic mud-grubbers with poor swimming capabilities, and low  
32 manoeuvrability [9–12]. Using computational fluid dynamics, we show that osteostracan  
33 headshield morphology is compatible with a diversity of hydrodynamic efficiencies  
34 including passive control of water flow around the body; these could have increased  
35 versatility for adopting diverse locomotor strategies. Hydrodynamic performance varies  
36 with morphology, proximity to the substrate and angle of attack (inclination). Morphotypes  
37 with dorsoventrally oblate headshields are hydrodynamically more efficient when  
38 swimming close to the substrate, whereas those with dorsoventrally more prolate  
39 headshields exhibit maximum hydrodynamic efficiency when swimming free from  
40 substrate effects. These results suggest different hydrofoil functions among osteostracan  
41 headshield morphologies, compatible with ecological diversification and undermining the  
42 traditional view that jawless stem-gnathostomes were ecologically constrained [9–12] with  
43 the origin of jaws as the key innovation that precipitated the ecological diversification of  
44 the group [13,14].

45

## 46 RESULTS

47 The origin of vertebrates can be characterised by increased cephalisation and a number of  
48 developmental and anatomical innovations rooted in whole genome duplication, increased

49 gene regulation, and the diversification of neural crest cell fates [15–17]. The ecological  
50 context to this formative evolutionary episode is envisioned as successive evolutionary grades  
51 of invertebrate chordates, jawless vertebrates and jawed vertebrates, exhibiting an overall  
52 trend towards increasingly active food acquisition that culminated in the active predatory  
53 ecology of extant gnathostomes [3,4]. In this scenario, the extinct jawless ‘ostracoderms’ are  
54 interpreted as cumbersome deposit feeders lacking key apomorphies of jawed vertebrates  
55 including multiple pairs of appendages and an epicercal tail, as well as jaws. This popular  
56 scenario belies the challenge of constraining the biology of ostracoderms which lack living  
57 analogues, traditionally compromising attempts to derive functional interpretations of their  
58 morphology [18]. However, the development of non-destructive tomographic methods for  
59 characterizing morphology, combined with computational engineering approaches that can  
60 be used to analyse quantitatively the functional performance of biological structures [19,20],  
61 render such macroecological and macroevolutionary hypotheses testable.

62

63 To this end, we analysed the functional morphological diversity of the Silurian–Devonian  
64 Osteostraci, the jawless sister group to all jawed vertebrates, which cover all the  
65 morphological grades exhibited by ostracoderms, including forms which entirely lack paired  
66 appendages and others that possess just a single (pectoral) pair (Figure 1a). The generic semi-  
67 circular, dorsoventrally flattened (oblate) osteostracan headshield has conventionally been  
68 interpreted as an adaptation to a sedentary benthic ecology [10,11,21–24]. However,  
69 osteostracan cranial morphology exhibits greater morphological disparity, including:  
70 morphotypes that are laterally compressed (prolate) and lack pectoral fins, interpreted as  
71 adaptations for burrowing, as well as forms with lateral and rostral expansions of the  
72 headshield, interpreted as adaptations for stabilization, enhancing lift or reducing drag

73 [12,23,25], deterring predators [26], housing sense organs [27], substrate anchoring [28], or  
74 specialised feeding strategies [29]. Using geometric morphometrics, we characterized  
75 quantitatively the morphological diversity of osteostracan headshields and derived an  
76 empirical morphospace that we interrogated using computational fluid dynamics (CFD) to  
77 determine how variation in morphological disparity correlates to aspects of hydrodynamic  
78 performance. CFD allowed us to simulate the interaction between flow and digital models of  
79 osteostracan morphology in three dimensions, exploring not only the impact of differences in  
80 morphology, but also the attitude of the organism with respect to flow (angle of attack) and  
81 its position relative to the substrate. We explored the fluid flow and forces generated over  
82 static models, interpreting the results exclusively in terms of morphological variation and  
83 assuming comparable modes of locomotion and post-cranial morphology for all species. The  
84 post-cranial anatomy of osteostracans is relatively conservative [18] and, hence, our  
85 morphospace analysis focussed on the headshields. In this way, we were able to test  
86 competing hypotheses of osteostracan ecology based on hydrodynamic performance criteria  
87 (such as the lift-to-drag ratio).

88

89 We characterised headshield morphology for 30 species belonging to 29 different genera and  
90 representing all major groups and the systematic breadth of osteostracans, using 123  
91 landmarks of type I–III (Figure 1b), which were subjected to Procrustes and pairwise distance  
92 analysis prior to ordination. The ensuing phylomorphospace conveys the relationship  
93 between phylogeny and morphological variation (Figure 1c), revealing widespread  
94 convergence evidenced by many pairs of taxa that are morphologically more similar than  
95 either are to their last shared ancestor. We applied CFD to eight taxa sampled from the limits  
96 of morphospace occupation, as well as the most common morphologies (Figure 1c).

97

98 We simulated both pelagic and benthic conditions with an inlet velocity of  $0.3 \text{ m s}^{-1}$ . In the  
99 pelagic scenario, eight different angles of attack were simulated at  $10^\circ$  intervals between  $0^\circ$   
100 and  $70^\circ$ . In the benthic scenario, the models were positioned at three different distances  
101 above the substrate (0.1, 0.5 and 1 body lengths) (Figure 1d). This combination of parameters  
102 covers a wide range of hypothetical modes of life, allowing us to interpret the hydrodynamic  
103 performance of osteostracan headshield under different ecological scenarios. Results of the  
104 simulations were interpreted both qualitatively, by visualizing the pressure distribution at the  
105 surface of the body, and quantitatively, by calculating drag and lift coefficients, and lift-to-  
106 drag ratios.

107

108 Sensitivity analyses demonstrate that the CFD results are independent of domain and mesh  
109 size (see Data S1 and STAR Methods section, respectively). The distributions of pressure over  
110 the body vary considerably between the pelagic and benthic simulations (Figure 2). In the  
111 pelagic simulations, the highest pressures are restricted to the front of the snout, whereas in  
112 the benthic simulations they occur along part of the ventral surface of the headshield. These  
113 differences are especially extreme in dorsoventrally compressed morphotypes, such as  
114 *Stensiopelta* (Figure 2F) and *Boreaspis* (Figure 2H).

115

116 The drag coefficient ( $C_D$ ) increases with the angle of attack and proximity to the substrate  
117 (Figure 3 and Table S1), showing a positive correlation with the degree of development of  
118 headshield cornual processes, in both benthic and pelagic scenarios at low angles of attack  
119 (i.e., from  $0^\circ$  to  $20^\circ$ ). Under pelagic conditions, the lift coefficient ( $C_L$ ) increases approximately  
120 linearly with angle of attack from  $0^\circ$  to  $30^\circ$  (Figure 3 and Table S1), exhibiting a significant

121 correlation with headshield morphology at low angles of attack (i.e., from 0° to 20°) where  
122 the highest values are attained by the morphotypes that are more triangular in outline.  $C_L$   
123 achieves its acme at 40°-50° before reaching the critical or stall angle of attack, at which point  
124  $C_L$  experiences an abrupt decrease. In the benthic scenario,  $C_L$  increases greatly for all  
125 morphotypes when they are located close to the substrate, but this effect is especially  
126 pronounced in taxa with oblate headshields; otherwise, there is no significant correlation with  
127 headshield shape. Absolute lift force generally overcomes apparent weight for all taxa at  
128 realistic angles of attack (between 10° and 30°) and cruising swimming speeds ( $0.30 \text{ m s}^{-1}$ ) in  
129 the pelagic scenario (Table S1). Moreover, the extra lift force generated when the models are  
130 located close to the substrate is enough to counteract the apparent body weight for most of  
131 the species at an angle of attack of 0°. The ratio between the lift and drag coefficients (L/D)  
132 is widely considered as a good proxy for hydrodynamic efficiency, and this varies substantially  
133 among the different morphotypes and ecological scenarios in our study (Figure 3 and Table  
134 S1). Under the pelagic scenario, the maximum L/D is attained for all morphotypes at angles  
135 of attack between 20° and 30° (except for *Hoelaspis* where it is attained at 40°). Under  
136 benthic conditions, peak L/D is achieved for all morphotypes when they are located at 0.1  
137 body lengths above the floor. Most species with dorso-ventrally oblate headshields show the  
138 highest L/D under benthic scenarios, whereas more dorso-ventrally prolate morphotypes  
139 achieve peak L/D under pelagic conditions. Morphologically intermediate species do not show  
140 major differences between the two scenarios and *Hoelaspis* presents the lowest L/D values in  
141 all cases.

142

143 **DISCUSSION**

144 Our analyses indicate that osteostracans with oblate headshields were hydrodynamically  
145 more efficient (i.e., they maximized lift and minimized drag) when swimming close to the  
146 substrate, whereas prolate morphotypes exhibited maximum hydrodynamic efficiency when  
147 swimming in the water column above substrate effects. We also show that headshield  
148 morphology in several osteostracan species is compatible with passive control of  
149 hydrodynamic performance through ground effect, generating extra lift when swimming  
150 close to the substrate that overcame the apparent weight of the fish. This phenomenon is  
151 widely used by modern demersal taxa (e.g., flatfishes, skates and rays) to augment lift and  
152 counteract negative buoyancy when actively swimming near the bottom [30], occurring as a  
153 consequence of the distortion of the flow and the resulting increased pressure below the  
154 organism. Patterns of variation in surface pressure (Figure 2) and lift coefficients (Figure 3) for  
155 both pelagic and benthic scenarios are also compatible with these osteostracans benefitting  
156 from ground effect during active swimming. Some living armoured benthic fishes use similar  
157 strategies to counteract negative buoyancy, exploiting ground effect when moving close to  
158 the substrate and generating lift by increasing the angle of attack when swimming in more  
159 pelagic conditions [31]. This could also be the case for some osteostracans, especially species  
160 with oblate headshield morphologies that produce the most lift through ground effect. Oblate  
161 cambered bodies (i.e., those with flat ventral sides) might also reflect other lifestyle functions,  
162 such as benthic station-holding. On the other hand, hydrodynamic performances calculated  
163 for prolate species may reflect strictly pelagic live styles, even when swimming at  
164 comparatively low speeds and high angles of attack [32]. In this sense, there are well reported  
165 cases of pelagic living fishes, with body sizes and swimming speeds comparable to those of  
166 osteostracans, that are able to swim at high angles of attack to counteract negative buoyancy  
167 in the water column.



168

169 Our results suggest that the broad disparity and widespread convergence in headshield  
170 morphology exhibited by clades of stem-gnathostomes [18] can be explained as a  
171 consequence of their hydrodynamic and ecological disparity [12]. This interpretation relies on  
172 the assumption of a similar range of body densities for the analysed taxa. Analyses of extant  
173 species have shown that cephalofoil function can be complex, and its hydrodynamic role is  
174 controversial. In this sense, an alternative scenario of lift generation, compensating for higher  
175 density in taxa with larger bony carapaces, should be also considered. However, this view is  
176 challenged by the observation that more robust osteostracan headshield morphologies (e.g.,  
177 *Stensiopelta*) do not produce greater lift than taxa with more gracile headshields (e.g.,  
178 *Hemicyclaspis* or *Cephalaspis*) [33]. Thus, we provide experimental evidence compatible with  
179 both ecological diversification and exploration of complex morpho-functional hydrodynamic  
180 adaptations among jawless stem-gnathostomes. Indeed, our novel results, coupled with  
181 previous research in bioengineering [34] and functional morphology [35], further suggest that  
182 mechanisms for passively controlling flow around the body may be prevalent among these  
183 groups, where they would have conferred greater manoeuvrability and versatility than  
184 previously thought [9–12]. This calls into question the prevailing view that stem-  
185 gnathostomes were ecologically constrained prior to the emergence of jawed vertebrates and  
186 the scenario of a general trend towards increasingly active food acquisition [3,4]. In this light,  
187 the ecology of early vertebrates appears to have been more diverse and complex [36,37].  
188 Thus, we have presented evidence of adaptations to a range of different lifestyles and  
189 ecologies evolved among jawless stem-gnathostome groups before the origin of jaws,  
190 underpinning the later exploration of novel trophic strategies and enhanced locomotory  
191 capabilities that emerged with the evolution of jaws, pelvic fins and trunk musculature

192 [14,38,39].

193

#### 194 **ACKNOWLEDGEMENTS**

195 We acknowledge support from H2020 in the form of a Marie Skłodowska-Curie Individual  
196 Fellowship (H2020-MSCA-IF-2018-839636) (to HF). Additional funding was provided by  
197 Oxford University Museum of Natural History (to IAR). We thank two anonymous reviewers  
198 for providing thoughtful and valuable comments on the manuscript.

199

#### 200 **AUTHOR CONTRIBUTIONS**

201 P.C.J.D, H.G.F and H.B. devised the project. H.G.F., I.A.R. and C.M.P. designed and performed  
202 the simulations. V.S.L. performed the 3D modelling. H.G.F and P.C.J.D wrote the manuscript  
203 with the support of the other authors.

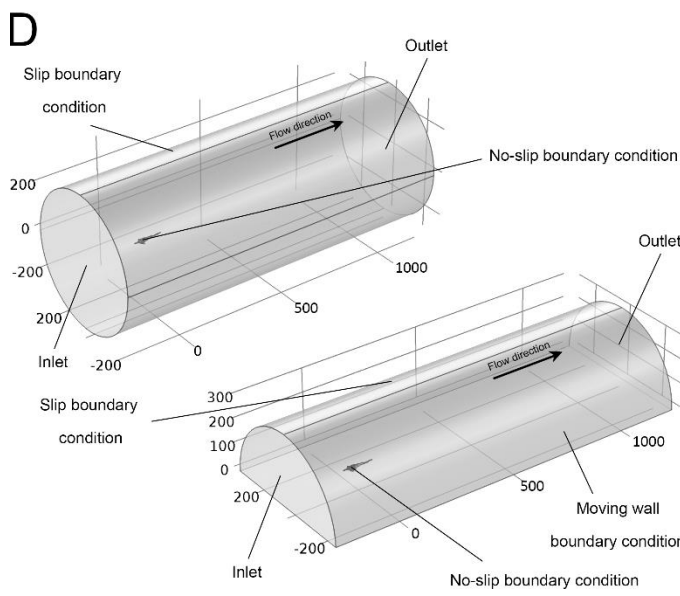
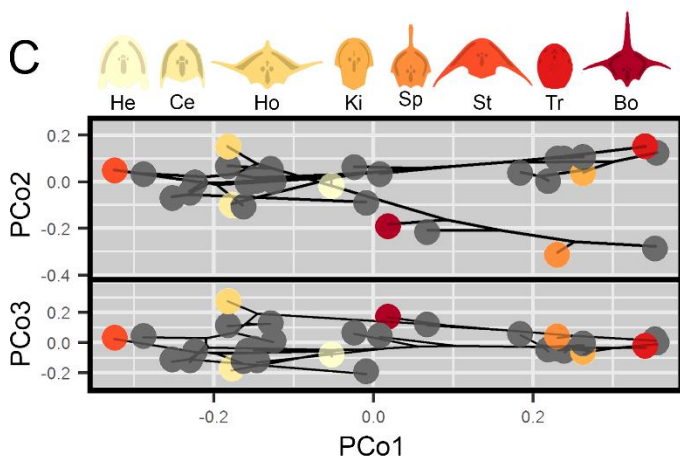
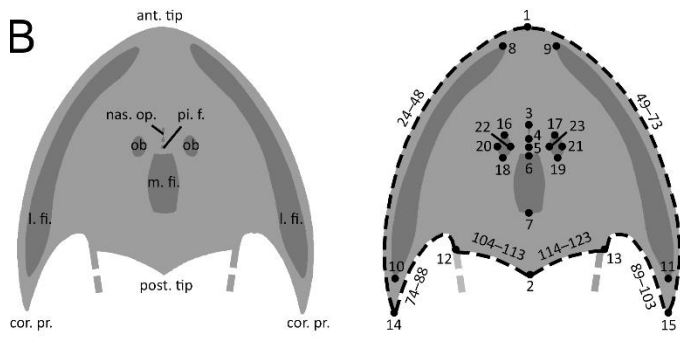
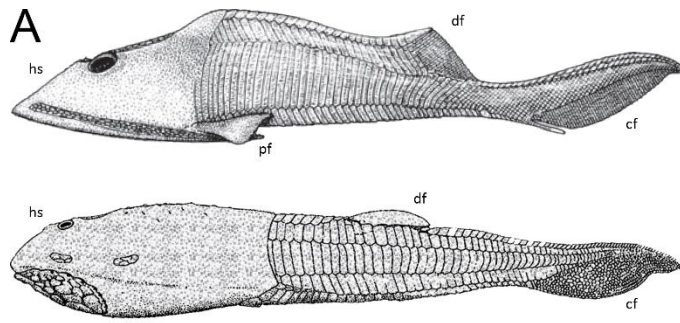
204

#### 205 **DECLARATION OF INTERESTS**

206 The authors declare no competing interests.

207

#### 208 **FIGURE LEGENDS**



210 **Figure 1. Morphology of osteostracans and experimental setup.** (A) General morphology of  
211 two well-known osteostracans, *Hemicyclaspis* (top) and *Tremataspis* (bottom), in lateral view,  
212 indicating the position of the pectoral fins (pf), dorsal fin (df), caudal fin (cf) and headshield  
213 (hs). Modified from Janvier [18]. (B) Descriptive diagrams showing anatomical characters of  
214 the osteostracan headshield (left) and the landmark configuration used in the geometric  
215 morphometric analysis (right). Landmark 1, anterior tip of the headshield or the rostral  
216 process (ant. tip.). Landmark 2, posterior tip of the headshield (post. tip.). Landmarks 3 and  
217 4, most anterior and most posterior medial points of the nasohypophysial opening (nas. op.)  
218 respectively. Landmark 5, pineal foramen (pi. f.). Landmarks 6 and 7, most anterior and most  
219 posterior medial points of the median field (m. fi.) respectively. Landmarks 8 and 9, most  
220 anterior points of the left and right lateral fields (l. fi.) respectively. Landmarks 10 and 11,  
221 most posterior points of the left and right lateral fields (l. fi.) respectively. Landmarks 12 and  
222 13, left and right points of connection between the headshield and the body respectively.  
223 Landmarks 14 and 15, left and right most distal points of the corneal processes (cor. pr.)  
224 respectively. Landmarks 16–23, most anterior, posterior, lateral and medial points of the eye  
225 orbits (ob.). Landmarks 24–73, type III landmarks situated between Landmarks 1 and 14 and  
226 between Landmarks 1 and 15. Landmarks 74–103, type III landmarks situated between  
227 Landmarks 14 and 12 and between Landmarks 15 and 13. Landmarks 104–123, type III  
228 landmarks situated between Landmarks 12 and 2 and between Landmarks 13 and 2. Modified  
229 from Ferrón et al. [41]. (C) Phylomorphospace summarizing the morphological diversity of  
230 osteostracan headshields. The proportion of variance explained by PCo1–3 are 62.46%,  
231 17.49% and 12.18% respectively. Taxa used in CFD analyses are highlighted in colour. Bo,  
232 *Boreaspis*; Ce, *Cephalaspis*; He, *Hemicyclaspis*; Ho, *Hoelaspis*; Ki, *Kiaeraspis*; Sp, *Spatulaspis*;  
233 St, *Stensiopelta*; Tr, *Tremataspis*. (D) Schematic illustration of the computational domain (i.e.,

234 all the objects around/through which the fluid will flow) used in CFD simulations for pelagic  
235 (upper) and benthic (lower) scenarios. All measurements in mm.

236

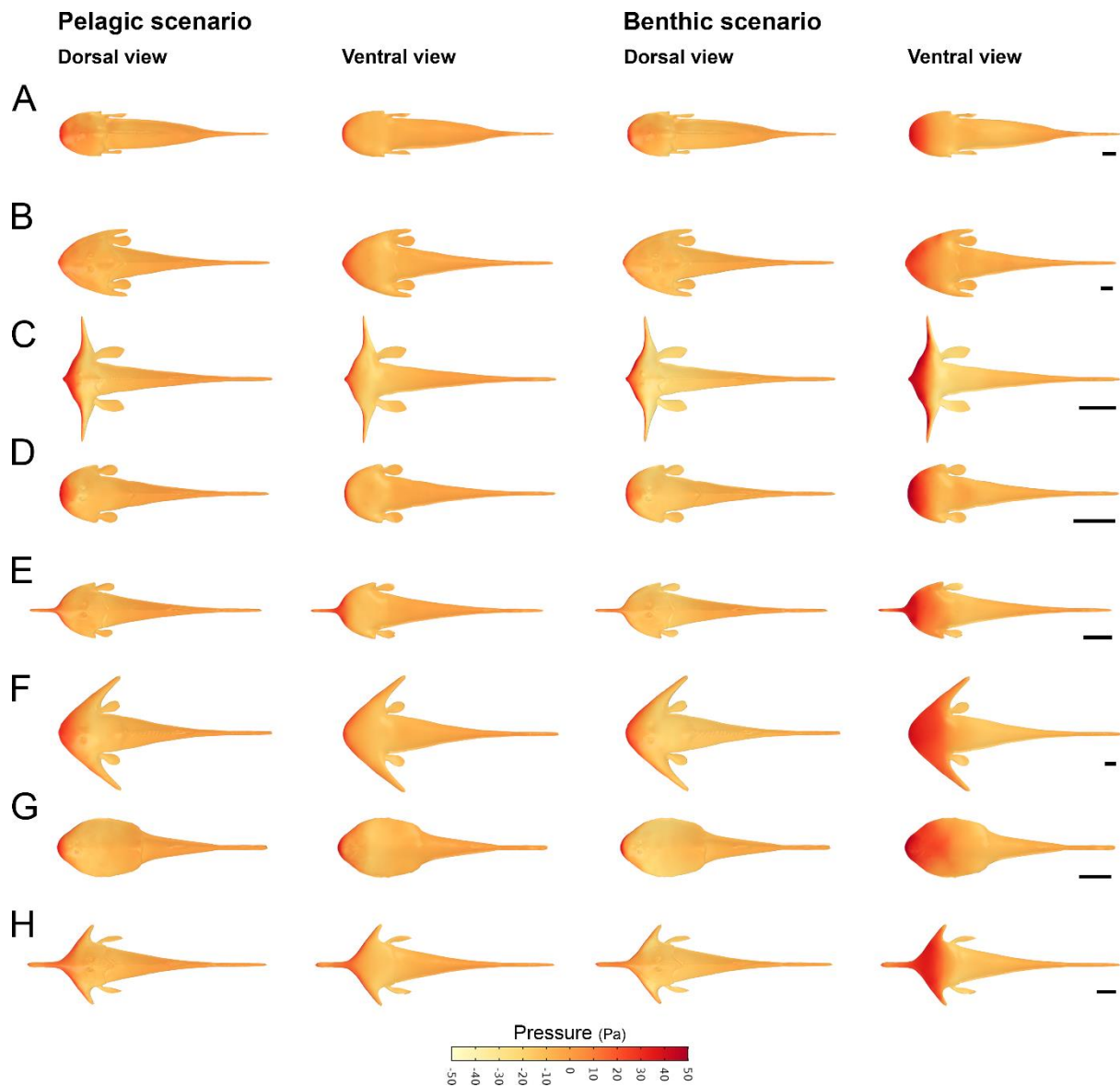
237

238

239

240

241



242

243

244

245

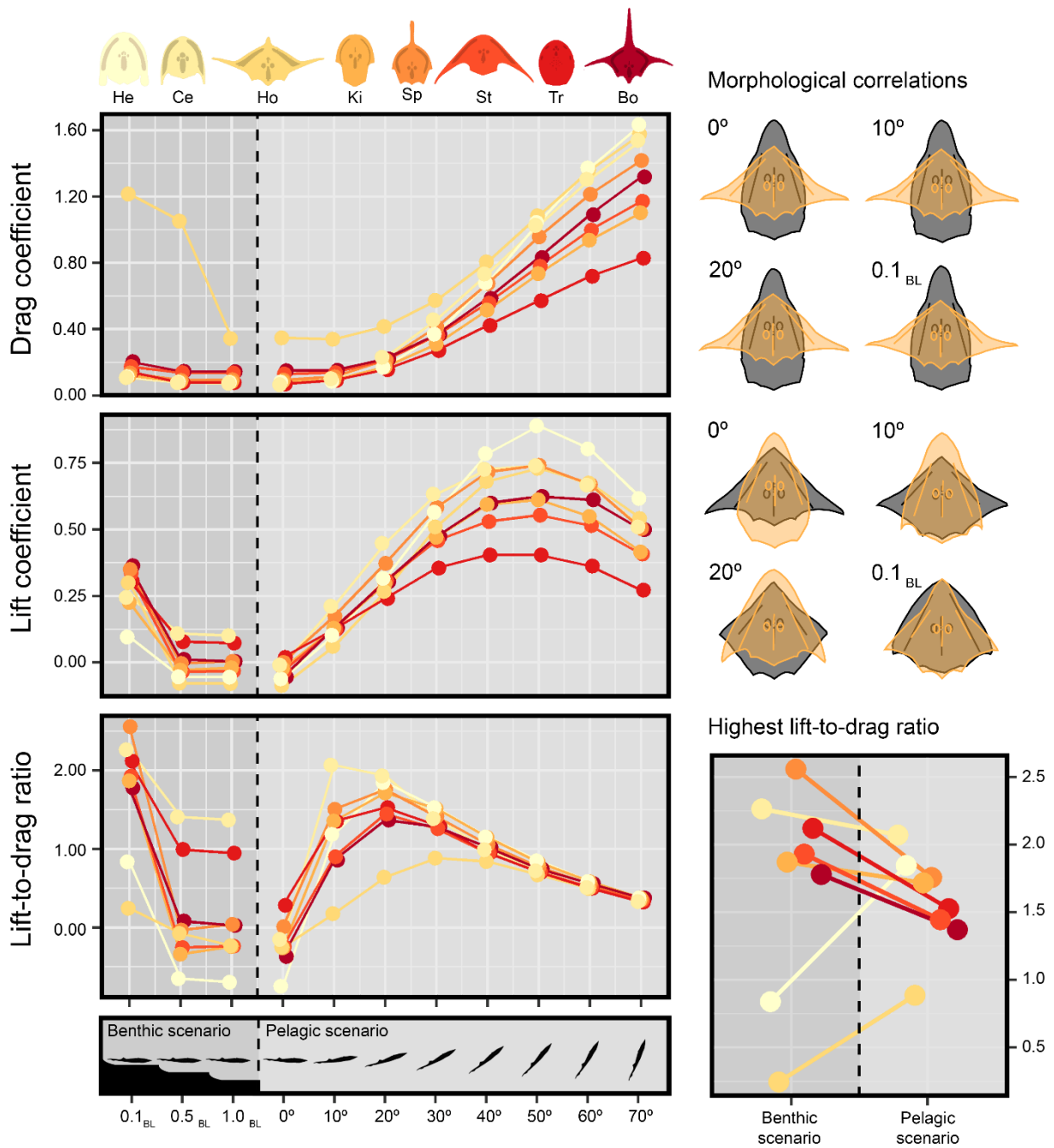
246

247

248

249

**Figure 2. Results of CFD simulations showing surface pressure distributions for osteostracan models under benthic (distance above the substrate of 0.1 body lengths) and pelagic scenarios (angle of attack of 0°) with an inlet velocity of 0.3 m s<sup>-1</sup>. (A) *Hemicyclaspis*. (B) *Cephalaspis*. (C) *Hoelaspis*. (D) *Kiaeraspis*. (E) *Spatulaspis*. (F) *Stensiopelta*. (G) *Tremataspis*. (H) *Boreaspis*. Note that models are lit from the top left to reveal their three-dimensional shape, but all of them display symmetrical pressure distribution patterns. Scale bar 2 cm.**



250

251

252

253

254

255

256

**Figure 3. Results of CFD simulations showing drag and lift coefficients and the lift-to-drag ratio, together with associated morphological correlations, under different experimental conditions (benthic scenario at 0.1, 0.5 and 1.0 body lengths (BL) above the substrate; and pelagic scenario at angles of attack of 0°–70°) with an inlet velocity of 0.3 m s<sup>-1</sup>. Data represented by points correspond to measured values. In the top right panel, grey and orange landmark wireframe configurations represent headshield morphologies with higher and**

257 lower force coefficients, respectively. Correlation results:  $C_D$  ( $0^\circ$ ): % predicted = 42.28, p-value  
258 = 0.0005;  $C_D$  ( $10^\circ$ ): % predicted = 42.16, p-value = 0.0001;  $C_D$  ( $20^\circ$ ): % predicted = 41.06, p-  
259 value = 0.0003;  $C_D$  ( $0.1_{BL}$ ): % predicted = 34.28, p-value = 0.0077;  $C_L$  ( $0^\circ$ ): % predicted = 42.15,  
260 p-value = 0.0012;  $C_L$  ( $10^\circ$ ): % predicted = 21.07, p-value = 0.0544;  $C_L$  ( $20^\circ$ ): % predicted =  
261 22.48, p-value = 0.0518;  $C_L$  ( $0.1_{BL}$ ): % predicted = 3.01, p-value = 0.6921. Bo, *Boreaspis*; Ce,  
262 *Cephalaspis*; He, *Hemicyclaspis*; Ho, *Hoelaspis*; Ki, *Kiaeraspis*; Sp, *Spatulaspis*; St, *Stensiopelta*;  
263 Tr, *Tremataspis*. See also Table S1.

264

## 265 **STAR METHODS**

266

## 267 **RESOURCE AVAILABILITY**

### 268 **Lead contact**

269 Further information and requests for resources should be directed to and will be fulfilled by  
270 the Lead Contact, Humberto G. Ferron ([Humberto.Ferron@bristol.ac.uk](mailto:Humberto.Ferron@bristol.ac.uk)).

271

### 272 **Materials Availability Statement**

273 This study did not generate new unique reagents.

274

### 275 **Data and code availability**

276 The datasets generated during this study are available at the Bristol Research Data Facility  
277 (<https://data.bris.ac.uk/data/dataset/1bjnv53uzx5dm2nw0q2tdtbqji>).

278

## 279 **EXPERIMENTAL MODEL AND SUBJECT DETAILS**

### 280 **Geometric morphometric analysis**



281 We limited our study to species of established taxa and conducted analyses at generic level,  
282 with each genus represented by a single specimen. We used the type species and holotype  
283 specimen for each genus except where this specimen was poorly preserved; in such cases,  
284 another well-defined species was used instead. We included a total of 30 specimens in the  
285 analysis, some of which exhibited minor deformation due to dorso-ventral compression  
286 (Table S2). This deformation was not corrected for due to the difficulties in doing so without  
287 introducing additional sources of error; previous work has demonstrated that biological signal  
288 is still retained when deformation is minor [40]. Images of specimens for digitization were  
289 obtained from photographs or published reconstructions (Data S2).

290

## 291 **METHOD DETAILS**

### 292 **Geometric morphometric analysis**

293 The morphological diversity of osteostracan headshields was summarized and numerically  
294 described using geometric morphometrics, following the procedure detailed in Ferrón et al.  
295 [41]. We digitized a total of 123 landmarks of type I, II and III on selected images using TpsDig  
296 v.2.26 [42] (Figure 1b). Type III landmarks were equally interpolated along the specimen  
297 outline in six different open curves. The number of Type III landmarks chosen to represent  
298 each curve was determined visually, reflecting the complexity and relative length of each part  
299 of the headshield. Variation in translation, rotation and size from the original landmark  
300 configurations was removed by generalized Procrustes analysis (GPA) in MorphoJ v. 1.06d  
301 [43] without implementing sliding methods for Type III landmarks. This choice is fully justified  
302 as sliding and non-sliding semilandmark methods provide similar superimpositions and PCA  
303 morphospaces (Figure S1 and Table S3) [44]. Distance matrices were obtained considering  
304 Euclidean distances and subjected to principal coordinate analysis in the packages ‘cluster’

305 [45] and 'ape' [46] in R [47]. Morphospaces and phylomorphospaces were constructed using  
306 the R packages 'Phytools' [48] and 'ggplot2' [49] based on pre-ordination ancestral state  
307 estimation [50]. Ancestral state reconstruction was achieved through stochastic character  
308 state mapping [51] using the R package 'geomorph' [52]. This analysis was based on the  
309 phylogenetic relationships proposed by Samson [53], after modification in Mesquite [54] and  
310 time-calibration in the R package 'paleotree' [55], according to the stratigraphic ranges  
311 published by Samson et al [56] (Data S3).

312

### 313 **Three-dimensional virtual modelling**

314 Eight species of osteostracans ("*Boreaspis*" *ceratops*, *Cephalaspis lyelli*, *Hemicyclaspis*  
315 *murchisoni*, *Hoelaspis angulata*, *Kiaeraspis auchenaspidoides*, *Spatulaspis robusta*,  
316 *Stensiopelta pustulata* and *Tremataspis schmidtii*), covering a good representation of all  
317 occupied regions of the morphospace (Figure 1c), were modelled virtually using 3D Studio  
318 Max (Data S4). Digital models obtained by three-dimensional virtual modelling have been  
319 shown to be reliable tools to assess function through computational analysis, providing very  
320 similar results to those derived from tomographic or surface-based techniques [57]. Here,  
321 modelling was based on photographs of fossil specimens and/or published reconstructions in  
322 multiple views (Table S4; see also Table S2 for a list of the specimens studied first hand).  
323 Complete headshields of all selected species are known and are usually preserved as three-  
324 dimensional structures, ensuring the accuracy of reconstructions. The postcranial region was  
325 accurately modelled for taxa in which it is known (i.e., *Cephalaspis* [58], *Hemicyclaspis* [59]  
326 and *Tremataspis* [60]), whereas a generalized osteostracan morphology was used for the  
327 remaining species. Spinal processes were represented on the dorsal line of the *Stensiopelta*  
328 model because these structures are known to be present in other zenaspidid osteostracans

329 [18]. Pectoral fins were modelled as paddle-like structures [61,62] and were positioned  
330 according to the location of the area of attachment. Digital reconstructions were scaled to life  
331 size using Netfabb Basic and converted into NURBS surface using Geomagic Studio.

332

### 333 **Computational fluid dynamics analyses**

334 Simulations of water flow around the three-dimensional osteostracan models were  
335 performed using COMSOL Multiphysics 5.2 ([www.comsol.com](http://www.comsol.com)). Two different computational  
336 domains were used to emulate pelagic and benthic conditions. For the pelagic scenario, the  
337 computational domain consisted of a three-dimensional cylinder (1500 mm in length and 300  
338 mm in diameter) in which the osteostracan model was centrally fixed and positioned at eight  
339 different angles of attack ( $0^\circ$  to  $70^\circ$ , every  $10^\circ$ ) (Figure 1d). For the benthic scenario, the  
340 computational domain consisted of a three-dimensional half-cylinder (1500 mm in length and  
341 300 mm in diameter) in which the osteostracan model was fixed at 0.1, 0.5 and 1.0 body  
342 lengths above the lower surface of the domain (Figure 1d). We evaluated the domain size to  
343 confirm it was sufficiently large that it did not influence fluid flow (Data S1).

344

345 An inlet with a normal inflow velocity boundary condition with a turbulence intensity of 0.05  
346 was defined at one end of the domain, and an outlet with a zero pressure boundary condition  
347 was specified at the opposing end. Boundaries at the top and sides of the domain were “open”  
348 (slip boundary condition), approximating flow through the domain, whereas the boundaries  
349 at the water–fossil interface were “solid” (no-slip boundary condition), fixing the fluid velocity  
350 at zero. The flat lower boundary of the half-cylinder used only in the benthic scenario was  
351 assigned a “moving wall” boundary condition, given the same velocity as the inlet. In all cases,  
352 an automatic wall treatment was used, with surface roughness not specified. The domain was

353 meshed using free tetrahedral elements and the ‘normal’ mesh size parameter in COMSOL  
 354 Multiphysics. To determine the influence of mesh size on the results of the CFD simulations,  
 355 we used three different meshes in an initial exploration of mesh quality for the *Kiaeraspis* and  
 356 *Stensiopelta* models, corresponding to the smallest and largest species, respectively. We  
 357 evaluated ‘coarser’ (maximum element size of 78.0 mm and minimum element size of 24.0  
 358 mm), ‘coarse’ (maximum element size of 60.0 mm and minimum element size of 18.0 mm),  
 359 and ‘normal’ (maximum element size of 40.2 mm and minimum element size of 12.0 mm)  
 360 meshes. In all cases, smaller elements were used in regions close to the fossil. Drag and lift  
 361 results obtained from normal and coarse meshes are very similar (see table below). As a result,  
 362 we selected a ‘normal’ mesh for use in our study because increasing the mesh quality further  
 363 would necessitate a large increase in computation time without any improvement in accuracy.  
 364 An inlet velocity of 0.3 m s<sup>-1</sup> was considered in all the cases.

365

366 *Kiaeraspis* (pelagic scenario, angle of attack 40°):

Mesh	Drag force (N)	Drag coefficient	Lift force (N)	Lift coefficient
Coarser	0.00689	0.51105	0.00758	0.56289
Coarse	0.00708	0.52508	0.00797	0.59177
Normal	0.00696	0.51669	0.00801	0.59467

367

368 *Stensiopelta* (pelagic scenario, angle of attack 40°):

Mesh	Drag force (N)	Drag coefficient	Lift force (N)	Lift coefficient
Coarser	0.10126	0.52276	0.09647	0.49802
Coarse	0.10719	0.55337	0.10427	0.5383
Normal	0.10808	0.55797	0.10267	0.53004

369

370 Three-dimensional, incompressible flow was simulated through the domain, with a stationary  
 371 solver used to compute the steady-state flow patterns. A realistic ambient flow velocity [63]

372 of  $0.30 \text{ m s}^{-1}$  was simulated (Reynolds numbers of 17100 to 64500). The Reynolds averaged  
373 Navier-Stokes (RANS) equations were solved using the shear stress transport (SST) turbulence  
374 model and a segregated solver algorithm; segregated iterations terminated when the relative  
375 tolerance (0.001) exceeded the relative error, computed as the minimum of the solution-  
376 based error and the error given by the Residual factor (1000) times the residual-based error.  
377 The effect of increasing inlet velocity was tested in parallel by simulating inlet velocities of  
378  $0.65$  and  $1.00 \text{ m s}^{-1}$  (Reynolds numbers of 37050 to 215000; Table S1).

379

380 The results were visualized as plots of pressure (Pa) over the surface of the osteostracan  
381 models. Drag and lift forces and their coefficients ( $C_D$  and  $C_L$ ) were calculated to quantify the  
382 flow around the digital reconstructions. For this, the headshield area was taken as the  
383 reference area. Apparent weight of each taxon was also calculated for comparative purposes  
384 assuming a body density of  $1100 \text{ kg m}^{-3}$  [64]. This value is in agreement with previous  
385 estimations on other ostracoderms considering the distribution and density of dermal bone,  
386 soft tissues and internal cavities [65]. All COMSOL Multiphysics files containing the  
387 simulations are available in the Bristol Research Data Facility  
388 (<https://data.bris.ac.uk/data/dataset/1bjnv53uzx5dm2nw0q2tdtbqji>).

389

## 390 **QUANTIFICATION AND STATISTICAL ANALYSIS**

391 Phylogenetic generalized least square (PGLS) analysis was undertaken in MorphoJ v. 1.06d  
392 [43] to test for correlations between shape changes and  $C_D$  and  $C_L$ . These analyses were  
393 performed for one benthic ( $0.1_{BL}$ ) and three pelagic (at  $0^\circ$ ,  $10^\circ$  and  $20^\circ$ ) scenarios, which were  
394 considered the most biologically realistic conditions. In all cases, we considered 0.05 as the  
395 level of statistical significance.

396

397 **SUPPLEMENTAL INFORMATION FILE LEGENDS**

398 **Data S1. Sensitivity analysis of domain size. Related to STAR Methods.**

399 **Data S2. Images used for the geometric morphometric analysis. Related to STAR Methods.**

400 **Data S3. R code and files used in the construction of the phylomorphospaces. Related to**  
401 **STAR Methods.**

402 **Data S4. Three-dimensional models used for the computational fluid dynamics analyses.**  
403 **Related to STAR Methods.**

404 **Table S1. Results of all CFD analyses performed for the eight selected species of**  
405 **osteostracans including details of how the Reynolds number, apparent weight, and the drag**  
406 **and lift coefficients and lift-to-drag ratios were calculated. Related to Figure 3.**

407

408 **REFERENCES**

409 1. Mallatt, J.O.N. (1984). Feeding ecology of the earliest vertebrates. *Zool. J. Linn. Soc.-*  
410 *Lond.* 82, 261–272.

411 2. Denison, R.H. (1961). Feeding mechanisms of Agnatha and early gnathostomes. *Am.*  
412 *Zool.* 1, 177–181.

413 3. Gans, C., and Northcutt, R.G. (1983). Neural crest and the origin of vertebrates: a new  
414 head. *Science* 220, 268–273.

415 4. Northcutt, R.G., and Gans, C. (1983). The genesis of neural crest and epidermal  
416 placodes: a reinterpretation of vertebrate origins. *Q. Rev. Biol.* 58, 1–28.

417 5. Gans, C. (1989). Stages in the origin of vertebrates: analysis by means of scenarios. *Biol.*  
418 *Rev.* 64, 221–268.

- 419 6. Mallatt, J. (1985). Reconstructing the life cycle and the feeding of ancestral vertebrates.  
420 In *Evolutionary Biology of Primitive Fishes*, R.E. Foreman, A. Gorbman, J.M. Dodd, and R.  
421 Olsson, eds. (New York and London: Plenum Press), pp. 59–68.
- 422 7. Mallatt, J. (1996). Ventilation and the origin of jawed vertebrates: a new mouth. *Zool. J.*  
423 *Linn. Soc.-Lond.* *117*, 329–404.
- 424 8. Mallatt, J. (1984). Early vertebrate evolution: pharyngeal structure and the origin of  
425 gnathostomes. *J. Zool.* *204*, 169–183.
- 426 9. Aleyev, Y., and Novitskaya, L.I. (1983). Experimental study of hydrodynamic qualities of  
427 Devonian heterostracans. *Palaeontol. J.* *1*, 3–12.
- 428 10. White, E.I., and Toombs, H.A. (1983). The cephalaspids from the Dittonian section at  
429 Cwm Mill, near Abergavenny, Gwent. *Bull. Br. Mus. Nat. Hist. (Geol.)* *37*, 149–171.
- 430 11. Belles-Isles, M. (1987). La nage et l'hydrodynamique de deux Agnathes du Paléozoïque:  
431 *Alaspis macrotuberculata* et *Pteraspis rostrata*. *Neues. Jahrb. Geol. P.-A.* *175*, 347–376.
- 432 12. Mark-Kurik, E. (1992). Functional aspects of the armour in the early vertebrates. In *Fossil*  
433 *fishes as living animals*, E. Mark-Kurik, ed. (Tallin, Estonia: Academy of Sciences of  
434 Estonia), pp. 107–115.
- 435 13. Miles, R.S. (1969). Features of Placoderm Diversification and the Evolution of the  
436 Arthrodire Feeding Mechanism. *Earth Environ. Sci. Trans. R. Soc. Edinb.* *68*, 123–170.
- 437 14. Anderson, P.S., Friedman, M., Brazeau, M.D., and Rayfield, E.J. (2011). Initial radiation of  
438 jaws demonstrated stability despite faunal and environmental change. *Nature* *476*, 206–  
439 209.
- 440 15. Marlétaz, F., Firbas, P.N., Maeso, I., Tena, J.J., Bogdanovic, O., Perry, M., Wyatt, C.D., de  
441 La Calle-Mustienes, E., Bertrand, S., and Burguera, D. (2018). *Amphioxus* functional  
442 genomics and the origins of vertebrate gene regulation. *Nature* *564*, 64–70.

- 443 16. Heimberg, A.M., Cowper-Sal, R., Sémon, M., Donoghue, P.C., and Peterson, K.J. (2010).  
444 microRNAs reveal the interrelationships of hagfish, lampreys, and gnathostomes and the  
445 nature of the ancestral vertebrate. *Proc. Natl. Acad. Sci. U.S.A.* *107*, 19379–19383.
- 446 17. Donoghue, P.C., Graham, A., and Kelsh, R.N. (2008). The origin and evolution of the  
447 neural crest. *Bioessays* *30*, 530–541.
- 448 18. Janvier, P. (1996). *Early vertebrates* (Oxford: Clarendon Press).
- 449 19. Cunningham, J.A., Rahman, I.A., Lautenschlager, S., Rayfield, E.J., and Donoghue, P.C.  
450 (2014). A virtual world of paleontology. *Trends in ecology & evolution* *29*, 347–357.
- 451 20. Rahman, I.A. (2017). Computational fluid dynamics as a tool for testing functional and  
452 ecological hypotheses in fossil taxa. *Palaeontology* *60*, 451–459.
- 453 21. Bunker, S.J., and Machin, K.E. (1991). The hydrodynamics of cephalaspids. In  
454 *Biomechanics in evolution*, J.M.V. Rayner, and R.J. Wootton, eds. (Cambridge and New  
455 York: Cambridge University Press), pp. 113–129.
- 456 22. Janvier, P., and Lawson, J.D. (1985). Environmental framework of the diversification of  
457 the Osteostraci during the Silurian and Devonian. *Philos. Trans. R. Soc. B* *309*, 259–272.
- 458 23. Afanassieva, O.B. (1992). Some peculiarities of osteostracan ecology. In *Fossil fishes as*  
459 *living animals*, E. Mark-Kurik, ed. (Tallin, Estonia: Academy of Sciences of Estonia), pp.  
460 61–70.
- 461 24. Morrissey, L.B., Braddy, S.J., Bennett, J.P., Marriott, S.B., and Tarrant, P.R. (2004). Fish  
462 trails from the lower old red sandstone of Tredomen Quarry, Powys, southeast Wales.  
463 *Geol. J.* *39*, 337–358.
- 464 25. Dec, M. (2019). Hydrodynamic performance of psammosteids: New insights from  
465 computational fluid dynamics simulations. *Acta Palaeontol. Pol.* *64*, 679–684.



- 466 26. Janvier, P. (1997). Contribution à la connaissance de l'anatomie et de la systématique du  
467 genre *Boreaspis* Stensiö (Agnatha, Cephalaspidomorphi, Osteostraci), du Dévonien  
468 inférieur du Spitsberg. *Ann. Paleontol.* 63, 1–32.
- 469 27. Voichyshyn, V. (2006). New osteostracans from the Lower Devonian terrigenous  
470 deposits of Podolia, Ukraine. *Acta Palaeontol. Pol.* 51, 131–142.
- 471 28. Janvier, P. (1985). Les Céphalaspides du Spitsberg. Anatomie, phylogénie et  
472 systématique des Ostéostracés siluro-dévonien. Révision des Ostéostracés de la  
473 formation de Wood Bay (Dévonien inférieur du Spitsberg) (Paris: CNRS édition).
- 474 29. Dineley, D.L. (1994). Cephalaspids from the Lower Devonian of Prince of Wales Island,  
475 Canada. *Palaeontology* 37, 61–70.
- 476 30. Vogel, S. (1994). *Life in moving fluids: the physical biology of flow* (Princeton: Princeton  
477 University Press).
- 478 31. Nowroozi, B.N., Strother, J.A., Horton, J.M., Summers, A.P., and Brainerd, E.L. (2009).  
479 Whole-body lift and ground effect during pectoral fin locomotion in the northern  
480 spearnose poacher (*Agonopsis vulsa*). *Zoology* 112, 393–402.
- 481 32. He, P., and Wardle, N.C. (1986). Tilting behaviour of the Atlantic mackerel, *Scomber*  
482 *scombrus*, at low swimming speeds. *Journal of Fish Biology* 29, 223–232.
- 483 33. Afanassieva, O.B. (2018). Morphogenetic Features of the Exoskeleton in Early Jawless  
484 Vertebrates (Osteostraci, Agnatha): Geometry of the Shield Sections. *Paleontol. J.* 52,  
485 1756–1763.
- 486 34. Botella, H., and Fariña, R.A. (2008). Flow pattern around the rigid cephalic shield of the  
487 Devonian agnathan *Errivaspis waynensis* (Pteraspidiformes: Heterostraci). *Palaeontology*  
488 51, 1141–1150.

- 489 35. Ferrón, H.G., and Botella, H. (2017). Squamation and ecology of thelodonts. *PloS one* 12,  
490 e0172781.
- 491 36. Purnell, M.A. (2001). Scenarios, selection, and the ecology of early vertebrates. In *Major*  
492 *events in early vertebrate evolution*, P.E. Ahlberg, ed. (London and New York: Taylor &  
493 Francis), pp. 188–208.
- 494 37. Purnell, M.A. (2002). Feeding in extinct jawless heterostracan fishes and testing  
495 scenarios of early vertebrate evolution. *Proc. R. Soc. B* 269, 83–88.
- 496 38. Anderson, P.S. (2008). Shape variation between arthrodire morphotypes indicates  
497 possible feeding niches. *J. Vertebr. Paleontol.* 28, 961–969.
- 498 39. Hill, J.J., Puttick, M.N., Stubbs, T.L., Rayfield, E.J., and Donoghue, P.C. (2018). Evolution  
499 of jaw disparity in fishes. *Palaeontology* 61, 847–854.
- 500 40. Angielczyk, K.D., and Sheets, H.D. (2007). Investigation of simulated tectonic  
501 deformation in fossils using geometric morphometrics. *Paleobiology* 33, 125–148.
- 502 41. Ferrón, H.G., Greenwood, J.M., Martínez-Pérez, C., Botella, H., Sansom, R.S., Deline, B.,  
503 and Donoghue, P.C.J. (in press.). Categorical versus geometric morphometric  
504 approaches to characterising the evolution of morphological disparity in Osteostraci  
505 (Vertebrata, stem-Gnathostomata). *Palaeontology*.
- 506 42. Rohlf, J. (2016). *tpsDig2*. v 2.26. Stony Brook University, New York.
- 507 43. Klingenberg, C.P. (2011). MorphoJ: an integrated software package for geometric  
508 morphometrics. *Mol. Ecol. Resour.* 11, 353–357.
- 509 44. Esteban-Trivigno, S.D. (2011). Ecomorfología de xenartros extintos: análisis de la  
510 mandíbula con métodos de morfometría geométrica. *Ameghiniana* 48, 381–398.
- 511 45. Maechler, M., Rousseeuw, P., Struyf, A., Hubert, M., and Hornik, K. (2019). *cluster*:  
512 *Cluster Analysis Basics and Extensions*. R package version 2.1.0.

- 513 46. Paradis, E., and Schliep, K. (2018). ape 5.0: an environment for modern phylogenetics  
514 and evolutionary analyses in R. *Bioinformatics* 35, 526–528.
- 515 47. R Development Core Team (2017). R: A language and environment for statistical  
516 computing. R Foundation for Statistical Computing, Vienna, Austria. 2016.
- 517 48. Revell, L.J. (2012). phytools: an R package for phylogenetic comparative biology (and  
518 other things). *Methods Ecol. Evol.* 3, 217–223.
- 519 49. Wickham, H. (2016). ggplot2: elegant graphics for data analysis (Springer).
- 520 50. Lloyd, G.T. (2018). Journeys through discrete-character morphospace: synthesizing  
521 phylogeny, tempo, and disparity. *Palaeontology* 61, 637–645.
- 522 51. Huelsenbeck, J.P., Nielsen, R., and Bollback, J.P. (2003). Stochastic mapping of  
523 morphological characters. *Syst. Biol.* 52, 131–158.
- 524 52. Adams, D.C., Collyer, M., Kaliontzopoulou, A., and Sherratt, E. (2019). Geomorph:  
525 Software for geometric morphometric analyses. R package version 3.1.0.
- 526 53. Sansom, R.S. (2009). Phylogeny, classification and character polarity of the Osteostraci  
527 (Vertebrata). *J. Syst. Palaeontol.* 7, 95–115.
- 528 54. Maddison, W.P., and Maddison, D.R. (2017). Mesquite: a modular system for  
529 evolutionary analysis. Version 3.2. <http://mesquiteproject.org>.
- 530 55. Bapst, D.W. (2012). paleotree: an R package for paleontological and phylogenetic  
531 analyses of evolution. *Methods Ecol. Evol.* 3, 803–807.
- 532 56. Sansom, R.S., Randle, E., and Donoghue, P.C. (2015). Discriminating signal from noise in  
533 the fossil record of early vertebrates reveals cryptic evolutionary history. *Proc. R. Soc. B*  
534 282, 20142245.
- 535 57. Rahman, I.A., and Lautenschlager, S. (2016). Applications of three-dimensional box  
536 modeling to paleontological functional analysis. *Pal. Soc. Pap.* 22, 119–132.

- 537 58. White, E.I. (1958). On *Cephalaspis lyelli* Agassiz. *Palaeontology* 1, 99–105.
- 538 59. Stensiö, E.A. (1932). The Cephalaspids of Great Britain (London: British museum, Natural  
539 History).
- 540 60. Janvier, P. (1985). Les Thyestidiens (Osteostraci) du Silurien de Saaremaa (Estonie).  
541 Première partie: Morphologie et anatomie. *Ann. Paleontol.* 71, 83–147.
- 542 61. Janvier, P. (1978). Les nageoires paires des Ostéostracés et la position systématique des  
543 Céphalaspidomorphes. *Ann. Paleontol.* 64, 113–142.
- 544 62. Janvier, P., Arsenault, M., and Desbiens, S. (2004). Calcified cartilage in the paired fins of  
545 the osteostracan *Escuminaspis laticeps* (Traquair 1880), from the Late Devonian of  
546 Miguasha (Québec, Canada), with a consideration of the early evolution of the pectoral  
547 fin endoskeleton in vertebrates. *J. Vert. Paleontol.* 24, 773–779.
- 548 63. Videler, J.J. (2012). *Fish swimming* (Salisbury, United Kingdom: Springer Science &  
549 Business Media).
- 550 64. Lowndes, A.G. (1955). Density of fishes: some notes on the swimming of fish to be  
551 correlated with density, sinking factor and load carried. *J. Nat. Hist.* 8, 241–256.
- 552 65. Botella, H. (2005). *Microictiolitos del Devónico Inferior de Nigüella (Cordillera Ibérica);*  
553 *consideraciones paleobiológicas e hidrodinámicas de condriactios y agnatos primitivos.*  
554 (Valencia: Universitat de Valencia).